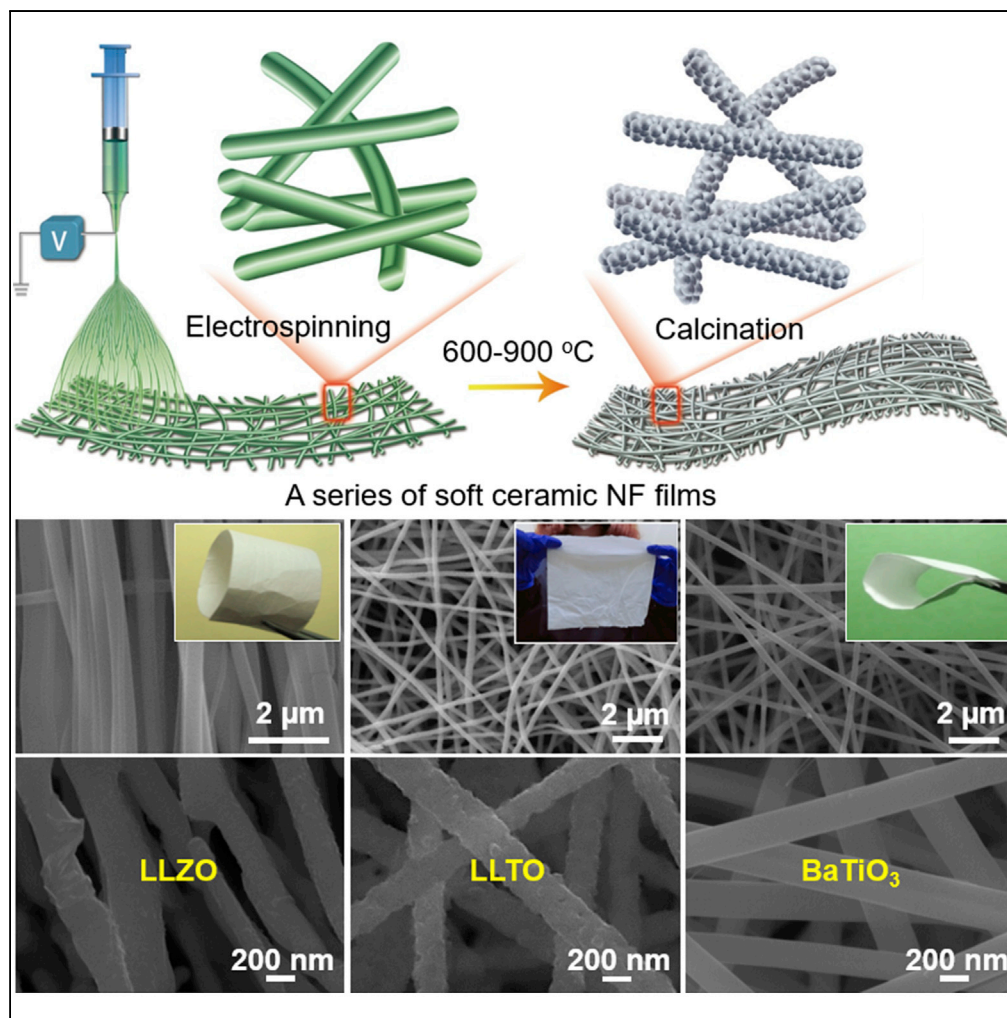**Article**

Polymer Template Synthesis of Soft, Light, and Robust Oxide Ceramic Films

Jianhua Yan, Yun Zhao, Xiao Wang, ..., Yuhui Han, Jianyong Yu, Bin Ding

yanjianhua@dhu.edu.cn (J.Y.)
binding@dhu.edu.cn (B.D.)

HIGHLIGHTS

A scalable method is developed for the fabrication of soft oxide ceramic films

A wide variety of soft, light, and robust oxide ceramic films are fabricated

A detailed soft deformation mechanism of the ceramic films is illustrated

The soft ceramic films exhibit appealing properties for applications

Article

Polymer Template Synthesis of Soft, Light, and Robust Oxide Ceramic Films

Jianhua Yan,[1,2,4,*] Yun Zhao,[1] Xiao Wang,[3] Shuhui Xia,[1] Yuanyuan Zhang,[1] Yuhui Han,[1] Jianyong Yu,[2] and Bin Ding[2,*]

SUMMARY

Oxide ceramic materials underpin a wide variety of technologies. However, the inherent fragility of these materials limits their use in emerging fields like wearable electronics and soft energy storage devices. Here, we develop a sol-gel electrospinning technique followed by calcination to create a range of oxide ceramic nanofiber films that exhibit significant softness without fragility after various deformations. This approach causes the ceramic crystals to fuse together at a low temperature during their growth within the polymer nanofiber templates. All the synthesized ceramic films, from SiO_2 to $BaTiO_3$, $Li_{0.33}La_{0.56}TiO_3$, and $Li_7La_3Zr_2O_{12}$, have silk-like softness of <31 mN, low density of <0.36 g/cm^3 and robust fire resistance to 1,000°C. Fabricated separators based on these films display large electrolyte uptakes of >900% and high thermal insulation performance, enhancing the rate capability and safety of lithium batteries. The reported method allows scalable synthesis of soft oxide ceramic films with properties appealing for applications.

INTRODUCTION

Oxide ceramics have been widely used in engineering and technology fields and enjoyed rapid development because of their superior properties such as robust mechanical strength, exceptional thermal and chemical stability, and physical integrity (Wu et al., 2016; Belmonte, 2006). Recently, researchers have successfully fabricated binary oxide ceramic films with shape memory performance, such as ZrO_2, TiO_2, and Al_2O_3 (Han et al., 2016, 2018; Cai et al., 2018). Such mechanical responses offer prospects to revolutionize diverse fields including electronics, energy, medical, aerospace, industrial manufacturing, and other fields and thus make soft oxide ceramics become hot favorites in the advanced material market. Among these applications, fabricating ceramic separators for advanced lithium (Li) batteries has attracted the attention of both academia and industry. Li-batteries provide efficient power for mankind in many applications, but they were prone to catch fire because of internal shorts (Tarascon and Armand, 2001).

Most battery internal shorts were potentially related to polymeric separators, which had limitations including low meltdown temperature, poor mechanical strength, and bad chemical inertness (Pan et al., 2017; Wang et al., 2018; Dai et al., 2016). During cycling, the excessive heating and the chemical oxidation as well as the mechanical attack by electrode expansion might damage the separators. Efforts to enhance the stability of separators have been focused on (1) fabricating ultrastrong separators with special polymers that could withstand high temperatures of 120°C–350°C (Jiang et al., 2013; Lin et al., 2016); (2) blending different polymers together to construct multicomponent separators, in which the polymer with the lowest melting point melted and clogged the permeating pores to turn off the battery operation in the case of excessive heating (Shi et al., 2015; Kim et al., 2016; Nunes et al., 2015; Liao et al., 2016; Costa et al., 2013); and (3) forming composite separators by filling or coating the polymeric separators with chemically and thermally stable ceramic particles (Prosini et al., 2002; Lee et al., 2014; Song et al., 2015; Kim et al., 2006; Xiao et al., 2018; Yu et al., 2014; Liu et al., 2017; Cho et al., 2017), which could improve thermal resistances and promote fast heat dissipation. These methods significantly improved the stability of polymer separators, but still had problems. For example, when thermal runaway occurred, the internal temperature of batteries would rapidly reach over 500°C, at which point the separators degraded immediately. On the other hand, the particles used as fillers or coating layers might block the pores and impede Li-ion transfer. In addition, the storage chemistry of Li-batteries is always accompanied by electrode volume changes, and

[1]Key Laboratory of Textile Science & Technology, Ministry of Education, College of Textiles, Donghua University, Shanghai 201620, China

[2]Innovation Center for Textile Science and Technology, Donghua University, Shanghai 200051, China

[3]State Key Laboratory for Modification of Chemical Fibers and Polymer Materials, College of Materials Science and Engineering, Donghua University, Shanghai 201620, China

[4]Lead Contact

*Correspondence: yanjianhua@dhu.edu.cn (J.Y.), binding@dhu.edu.cn (B.D.)

separators were thus always exposed to stress, in which situation the particles might flake off (Wang et al., 2016; Yanilmaz et al., 2016).

In this article, we propose a scalable and low-cost synthesis strategy to manufacture soft, light, and robust oxide ceramic separators with exceptional chemical and thermal stability. By developing a scalable ceramic nanofiber (NF) fabrication technique based on electrospinning and calcination, we fabricated a suit of soft ceramic NF films with controllable morphology and thickness including binary oxide of SiO_2, ternary oxide of $BaTiO_3$ (BTO), quaternary oxides of $Li_7La_3Zr_2O_{12}$ (LLZO), and $Li_{0.33}La_{0.56}TiO_3$ (LLTO). All these ceramic NF films displayed lightness of polymer (<0.36 g/cm^3) and softness of silk (stiffness of <31 mN). Here we demonstrated these four materials because they represented different types of oxide ceramics, offering a wide diversity in designing ionic pervious or conductive separators. Specifically, the SiO_2 had an amorphous structure, the BTO and LLTO had perovskite structures, whereas the LLZO had garnet structure. Soft ceramic separators like these would be extremely attractive for constructing high-safety Li-batteries that require separators to have both soft and hard properties.

These ceramic separators exhibited high liquid electrolyte uptakes of >900% and large electrolyte retention capability. In addition, they showed robust mechanical integrity that could be laminated securely to the electrodes. The batteries of NCA ($LiNi_{0.8}Co_{0.15}Al_{0.05}O_2$)//LLZO separator//Li with limited liquid electrolytes delivered a capacity increase of ~60 mA h/g at 0.5 C compared with the batteries containing the traditional polymer separators of Celgard 2,500. In addition, these batteries exhibited long cycling stability (80% of capacity retention over 600 cycles), good rate capability (0.1–1 C), abused temperature tolerance (100°C), and high voltage chemistry (2.7–4.6 V), demonstrating more advantages compared with the Celgard 2,500-based liquid-type batteries.

RESULTS

Material Fabrication and Characterization

Figure 1A proposes a general overview of the fabrication of soft oxide ceramic NFs using a sol-gel electrospinning method followed by calcination. The procedures involved the following three steps: (1) stable sol-gel precursor solutions are formed that contained polymer templates and the needed metal salts; (2) during the electrospinning process, with the electrical field changed from strong to weak, the spinning solutions undergo a process of rapid drawing and phase separation to form solidified polymer NF precursors; (3) in the subsequent calcination, accompanied by the decomposition of polymers was the formation of ceramic NFs, where the ceramic nanoparticles (NPs) go through a series of evolutions of crystal nucleus formation and crystal transition, as well as grain growth and fusion.

By carefully designing the electrospinning and calcination parameters, four types of ceramic NFs were prepared, as shown in Figure 1B. These ceramic films displayed intriguing shape memory performance and could maintain their original shapes after various deformations. These ceramic materials exhibited standard crystalline structures as checked by X-ray diffraction (XRD, Figure S1). The average NF diameters of the LLZO, LLTO, BTO, and SiO_2 were 251, 403, 331, and 489 nm, respectively (Figure S2). These NFs contained primary nanoscale grains, which were bonded with each other to form secondary particles, as verified by the transmission electron microscope (TEM) (Figure S3). Interestingly, when compared with the commercial polymeric separator of Celgard 2,500 that displayed a low electrolyte penetration ability, all the ceramic NF films exhibited markedly enhanced electrolyte wettability (Figure 1C) and ultralarge electrolyte uptakes of >900% (Figure S4). It is believed that ceramic NPs had strong interactions with the polar surface groups of the liquid electrolytes, enabling a fast electrolyte wicking speed and a high electrolyte retention ability (Xiang et al., 2011). After absorbing electrolytes, these soft ceramic NF films could be used as hybrid solid separators for high-chemistry Li-ion batteries.

To advance these ceramic separators into real applications, it is necessary to increase their areas and decrease their thickness substantially while maintaining the mechanical integrity. The thicknesses of these ceramic films were finely controlled below 50 μm (Figure S5). The film area could be scaled to 2,000 cm^2 (Figure 2A) with a medium spinning machine and 12,000 cm^2 (Figure S6) with a large spinning machine without compromising the mechanical softness. This large and thin ceramic film was soft enough to be folded into a ceramic crane (Figure 2B). To understand the softness and the durable robustness, bending stiffness and elastic modulus were measured (Figure 2C), where the commercial Celgard 2,500 films were
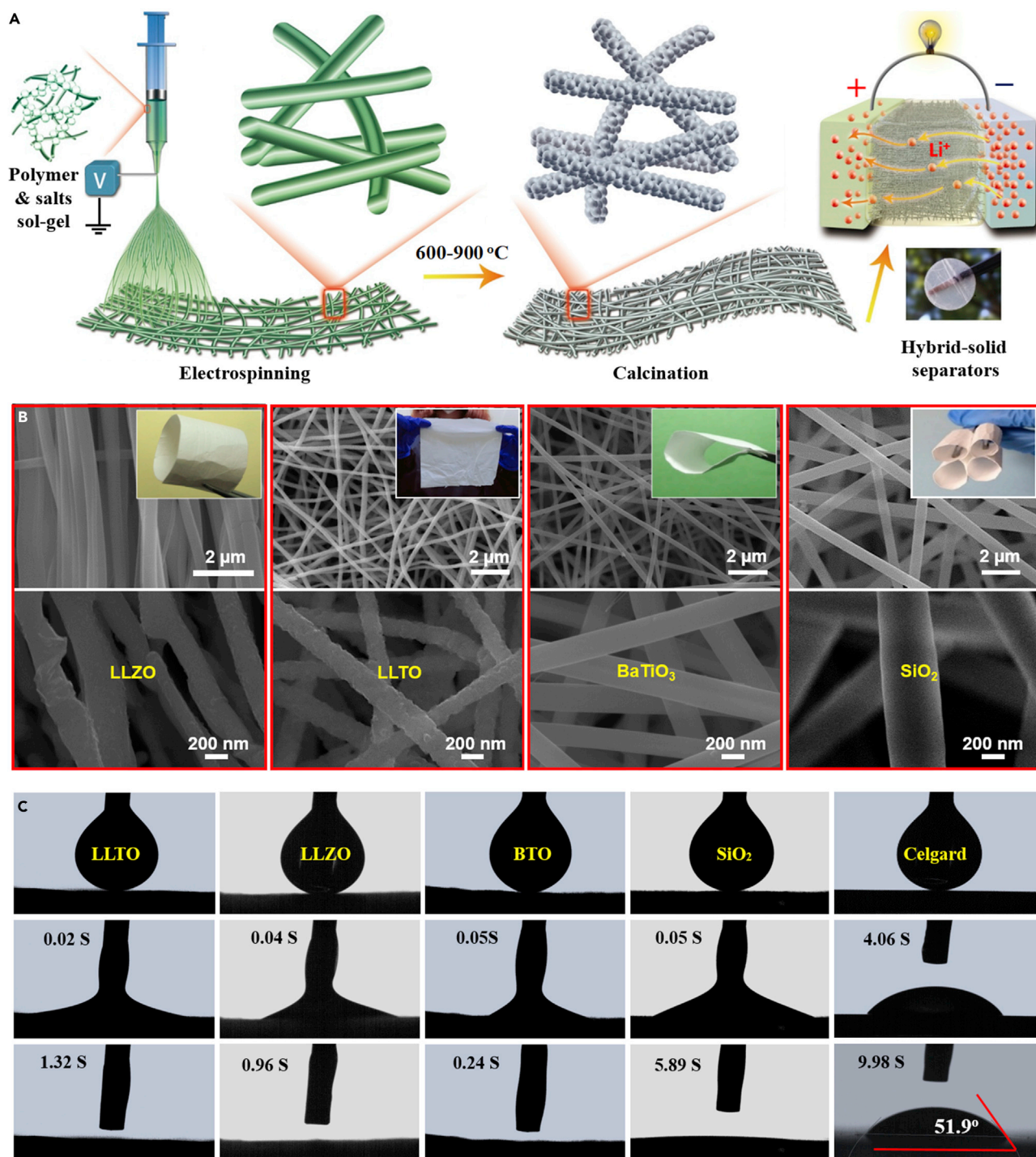
Figure 1. Fabrication Procedures, Morphological Characterizations, and Electrolyte Uptake Capability

(A) A general picture of using sol-gel electrospinning followed by calcination to fabricate ceramic NF separators for advanced Li-batteries.

(B) Morphology and mechanical softness of the electrospun ceramic NF membranes including LLZO, LLTO, BTO, and SiO$_2$.

(C) Electrolyte wettability of the ceramic NF separators and the commercial Celgard 2,500 separator.

tested as control samples. Here, the bending stiffness refers to the ability of the ceramic film (Figure 2D) or a single ceramic NF (Figure 2E) to resist the elastic deformation when being subjected to stresses, whereas the elastic modulus is the ratio of the stress to the strain in the transverse direction. All these ceramic films
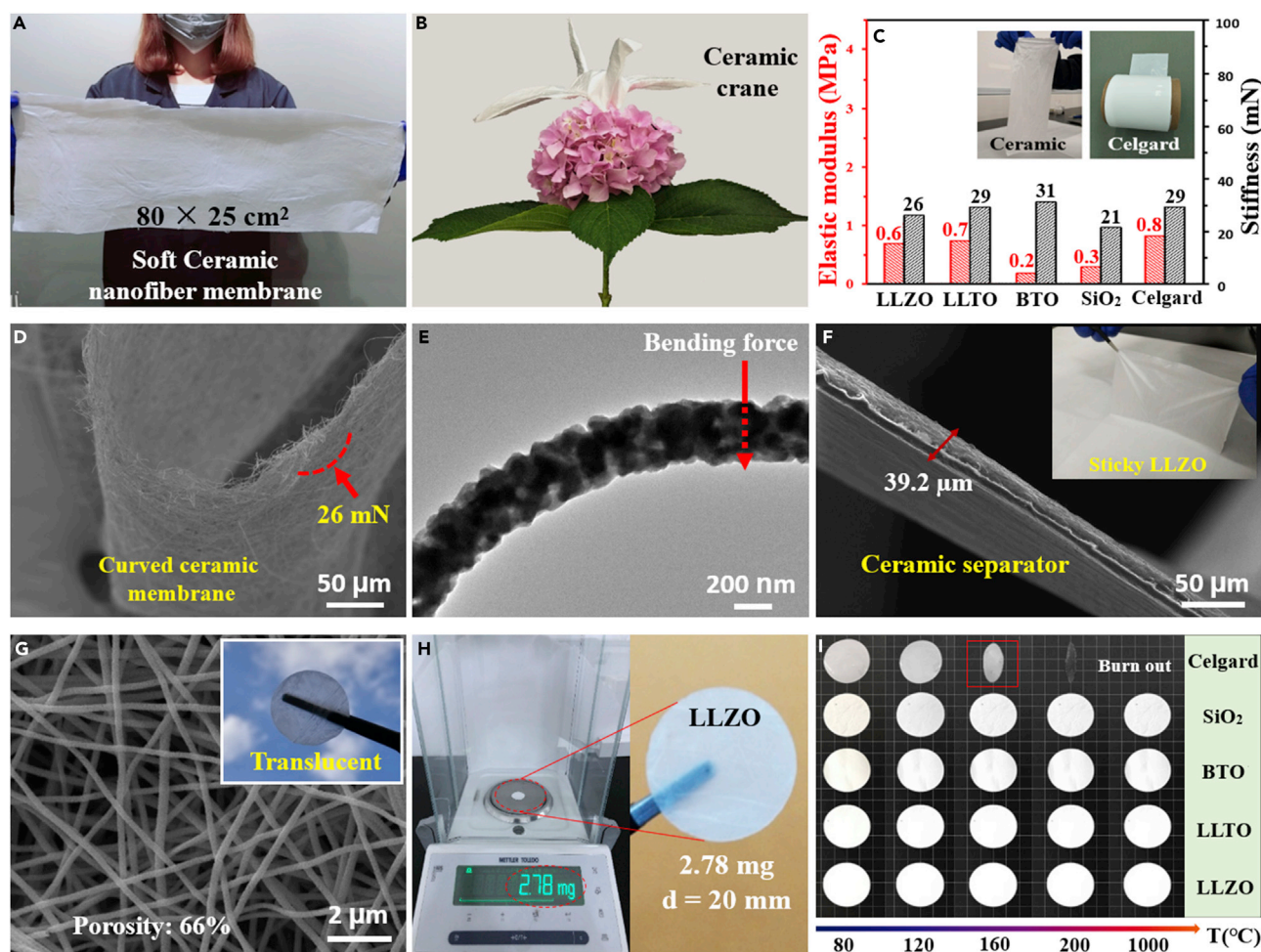
Figure 2. Physical and Thermal Characterizations of the Ceramic and Polymer Separators

(A and B) (A) A large-scale ceramic NF membrane and (B) a ceramic crane made from this film.

(C) Bending stiffness and elastic modulus tests.

(D and E) (D) The soft ceramic NF membrane and (E) a single ceramic NF at bending states.

(F) The fabricated soft ceramic LLZO NF membrane with a thickness of 39.2 μm.

(G) The soft ceramic LLZO NF membrane with a large porosity of 66% and translucent property.

(H) Weight of a circular LLZO separator.

(I) Comparison of thermal stability between the ceramic NF separators and the Celgard 2,500.
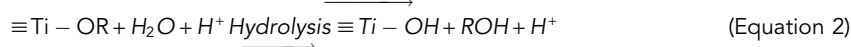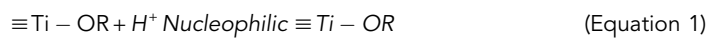
had better softness (smaller stiffness) while maintaining comparable elastic modulus when compared with the Celgard 2,500.

All these ceramic separators exhibited flyweight densities of <0.36 g/cm^3 (Figure S7) with light weights (Figure S8). In contrast, the Celgard 2,500 displayed a much higher volumetric weight of 0.43 g/cm^3, although it had a smaller thickness of ~25 μm (Figure S9A). The weight density was closely related to the degree of porosity. The Celgard 2,500 had a small porosity of 40%–50% (Figure S9B), whereas for a specific translucent LLZO NF film with a thickness of 39.2 μm (Figure 2F), the porosity reached 66% (Figure 2G). Such a high porosity rendered a circular LLZO separator with a light weight of 2.78 mg (Figure 2H), which was smaller than 3.05 mg of the Celgard 2,500. On the other hand, although the Celgard 2,500 had a larger elastic modulus at room temperature, it typically could not withstand high temperature (Figure S10). As shown in Figure 2I, the Celgard 2,500 started to deform at 80°C, while all the ceramic separators exhibited high thermal stability and maintained their shapes without shrinkage at 1,000°C. The thermogravimetric analysis curves further verified the high stability of these ceramics during the entire heating period from 30°C–1,000°C (Figure S11).

Strategies to Make Soft Oxide Ceramic NF Films

The softness of the ceramic NF films was determined by three key steps, as shown in Figure 3A. They were formation of stable sol-gel spinning solutions, electrospinning, and calcination. Here, we take LLTO as an example to illustrate our strategies to make soft multicomponent oxide ceramic NF films. The detailed information for synthesizing the other three ceramic materials are summarized in the Supplemental Information.

First, metal alkoxides of $C_{16}H_{36}O_4Ti$ were dissolved in a mixed solution of ethanol and acetic acid to form Ti network, which provided sufficient loading sites for La- and Li-ions. Then, the above salt solutions were mixed with polyvinyl pyrrolidone water solutions together to form stable sol-gel. Metal alkoxides were very active due to their negative alkoxy group, which made metal atoms vulnerable to nucleophilic attack. Hydrolysis and polymerization occur immediately after absorbing the water in air. When acetic acid was added as catalyst, the hydrolysis process was accelerated due to the nucleophilic attack of H^+ ions (as shown in Equations 1 and 2).

$$\equiv Ti - OR + H^+ \xrightarrow{Nucleophilic} \equiv Ti - OR \qquad \text{(Equation 1)}$$

$$\equiv Ti - OR + H_2O + H^+ \xrightarrow{Hydrolysis} \equiv Ti - OH + ROH + H^+ \qquad \text{(Equation 2)}$$

Here acetic acid played a dual role of catalysis and coordination substitution; the former accelerated, whereas the latter delayed the hydrolysis process. Therefore a stable sol could be obtained by controlling the amount of acetic acid. Then, La and Li salts were added into the above sol solution. Because of the strong negative electricity of acetate anion and the strong positive electricity of Ti in $C_{16}H_{36}O_4Ti$, it was likely that acetate radical would continuously replace the oxygen-butyl group to form bridge-bonded di-coordination group, as shown in Figure 3B. La, Li, and Ti were connected and interacted by acetate radical. These metal ions acted as a cross-linking agent between polymer chains, both of which led to the transformation of the sol-solution into sol-gel. The sol-gel methods endow these metal salts in the precursor solution with sufficient reaction in nanoscale.

After preparing the stable sol-gel that contained polymers and the needed salts, the dynamic evolution process of the solutions during the electrospinning process was investigated. After adding a large voltage (tens of thousands of volts) to the nozzle, an electric field was formed and the colloidal particles of salts that were wrapped by the polymers were charged at the nozzle (Figure 3C). Here polymers acted as soft templates to bind the salts together without separation in the electrical field. Under the combined action of the electric force and the electrostatic repulsion force, the colloidal solutions went through a process of rapid drawing and phase separation to form solidified polymer NF precursors. Of note, the air humidity had a great influence on the formation of NFs because the water in air would eliminate the charges of the spinning droplets.

The subsequent calcination procedures involved several complex changes that had strong dynamic dependence on time. The formation of crystalline ceramic NPs involved crystal nucleation, transition, growth, fusion, and polycrystalline NP formation. A rapid heating rate always resulted in discontinuous ceramic NFs, because the polymer would quickly decompose, but the crystals did not have enough time to grow. On the other hand, the smaller sizes and the larger quantities of the NPs made it easier to form continuous NFs. As the contents in the precursor NFs were fixed before the calcination, more nucleation would lead to more NPs and smaller NP sizes. Nucleation generally started at low temperatures, but the crystal growth and transition would occur at high temperatures. Therefore, based on the above analysis, our calcination strategy was to keep a proper crystal nucleation temperature for 3 h, during which period the polymers maintained their structures well without decomposition, and then slowly raise the heating rate to the calcination temperature for crystal growth.

Here, polymers were expected to act as grain size inhibitor and a bridge to promote grain interactions. First, due to the high surface atomic density and surface energy of these ceramic NPs, both the van der Waals forces and the interaction forces of chemical bonds between the NPs resulted in soft agglomerations of these NPs by point-to-point contacting. The smaller these NPs, the larger the adhesion forces from the soft agglomerations. Second, the *in situ* crystal growth would lead to the formation of crystal bridges at the very beginning of the crystallization, which caused the fusion of the adjacent crystals. During subsequent growth, the atoms on the surfaces of the NPs would diffuse into the adjacent NPs and form stable chemical
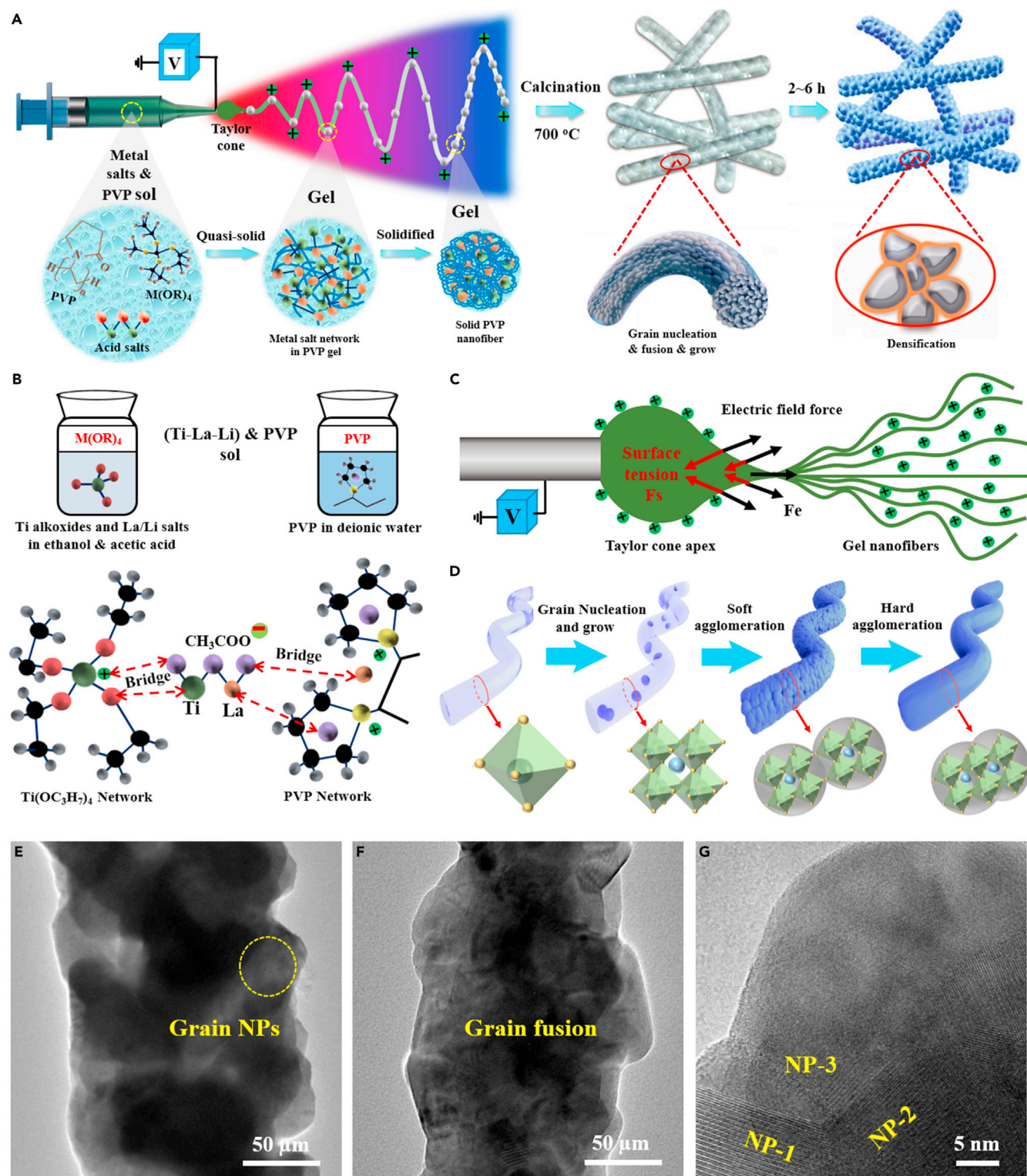
Figure 3. Mechanisms of Forming the Soft Oxide Ceramic NFs

(A) A general picture of using sol-gel electrospinning followed by calcination to fabricate oxide ceramic NF membranes.

(B) Schematic showing the sol-gel formation process and the interactions between the metal salts and polyvinyl pyrrolidone.

(C) Competition between the two main forces on the Taylor apex during electrospinning process.

(D) Schematic illustrating the grain changes during calcination in the polymer NF templates.

(E–G) TEM images of the ceramic NFs that demonstrate a series of evolutions of crystal nucleus formation, grain growth and grain fusion. (E) Grain growth, (F) grain fusion and (G) grain bounding during the calcination processes to form densely packed ceramic NPs in the NFs.

bonds, thus forming hard agglomerations between these NPs by surface-to-surface contacting (Figure 3D). Both the soft and hard agglomerations resulted in densely packed and continuous NP distributions in the NFs, as indicated from the TEM images (Figures 3E–3G).

The softness and robustness of the ceramic films were mainly endowed by the large length to diameter (L/D) ratio of the individual NFs and the staggered arrangement of NFs (Ge et al., 2016). The electrospun ceramic films had well-staggered and ultrahigh L/D ratio of NFs. When a bending stress was applied to the ceramic NF films, deformation occurred. On the other hand, the soft deformation mechanism of a single ceramic NF was different from that of the films. A straight loading force on the cross section of a single NF would cause the dislocation and recombination between these NPs due to the small attractive force of the soft agglomerations, thus scattering the concentrated stress and showing softness of the ceramic NFs, as indicated by the movements of NPs 1–4 (Figure S12), whereas the large adhesion force between these NPs existed as hard agglomerations endowing the ceramic NFs a certain mechanical strength without breaking. As shown in the atomic force microscopic surface structures (Figure S3B), the NP distributed continuously in the NFs and they bit each other like gears, which increased the binding forces and thus enhanced the robustness of the NFs. Of note, the movements of the ceramic NPs could not be automatically recovered, which means the ceramic NFs did not possess the property of elastic bending, but had a soft property like silk (Figure S13). Based on this analysis, a good strategy to enhance the softness of the ceramic NFs while maintaining their robust mechanical strength was to increase both the soft and hard agglomerations by decreasing the NP sizes while increasing the continuity of the ceramic NPs in the NFs.

Potential Applications of the Ceramic NF Films as Separators for Li-Batteries

The fabricated ceramic NF films had a high electrolyte retention capacity. As a lean electrolyte could substantially improve battery energy density and alleviate Li-dendrite growth (Qian et al., 2015; Zhang et al., 2018), the amounts of liquid electrolytes were therefore restricted to 4 μL/mg of cathodes (in NCA//ceramic//Li cells) or 10 μL (in steel||steel cells or Li||Li symmetric cells and Li||Cu asymmetric cells).

The ionic conductivity of these ceramic separators and a Celgard 2,500 separator at room temperature were measured by electrochemical impedance spectroscopy, which was performed on electrolyte-infiltrated separators sandwiched between two stainless-steel plates. The bulk resistances were obtained from the intersection coordinates of the data lines and the z′ axis (Figure 4A). All these ceramic separators had a small bulk resistance of $<10 \, \Omega/cm^2$. The corresponding ionic conductivities were calculated and summarized in Table S1. The low ionic resistances of these ceramics were potentially related to their ability of efficient wetting with electrolytes and the large electrolyte retention capacity, which facilitated migrations of Li-ions between electrodes. In addition, the strong interactions of the polar surface groups of the liquid electrolytes with the ceramic NPs also created additional Li-ion conduction pathways.

Such efficient Li-ion conductive ceramic separators enabled long-term Li plating (3 h) and stripping (3 h) of cycling stability in Li||Li symmetric cells for at least 700 h, which were evaluated at room temperature under three alternately applied current densities (Figure 4B). Here we demonstrated the ceramic LLZO separators as an example. At $0.1 \, mA/cm^2$, the voltage gap (i.e., between plating and stripping cycles) gradually decreased from 8 to 5.5 mV within 156 h. The decrease was ascribed to the improved Li-ion permeability after several cycles. When the current density was increased to $0.2 \, mA/cm^2$, the voltage gap was maintained at ~12 mV in the entire test period of 486 h, indicating a stable overall resistance of the LLZO separator during cycling. When the current density was increased to $0.6 \, mA/cm^2$, the cells could run normally and the voltage gap was expanded to 50 mV.

The LLZO separator also enabled a great improvement in Coulombic efficiency (CE) and the duration of Li||Cu asymmetric cells. A stable CE value close to 95% with a small fluctuation was obtained at $0.2 \, mA/cm^2$ over the entire 150 cycles (Figure 4C). In contrast, the Celgard 2,500 cell displayed a small initial CE value of ~90% and it quickly dropped after 135 cycles with a larger fluctuation all the way. The fluctuation of CE plots was probably associated with the formation of "dead or dendrite Li." When increasing the current density to $0.5 \, mA/cm^2$, the LLZO separator also exhibited a high and stable CE value of 97.5% within 150 cycles; however, the Celgard cell had a low CE value and started to quickly degrade after 60 cycles (Figure 4D).
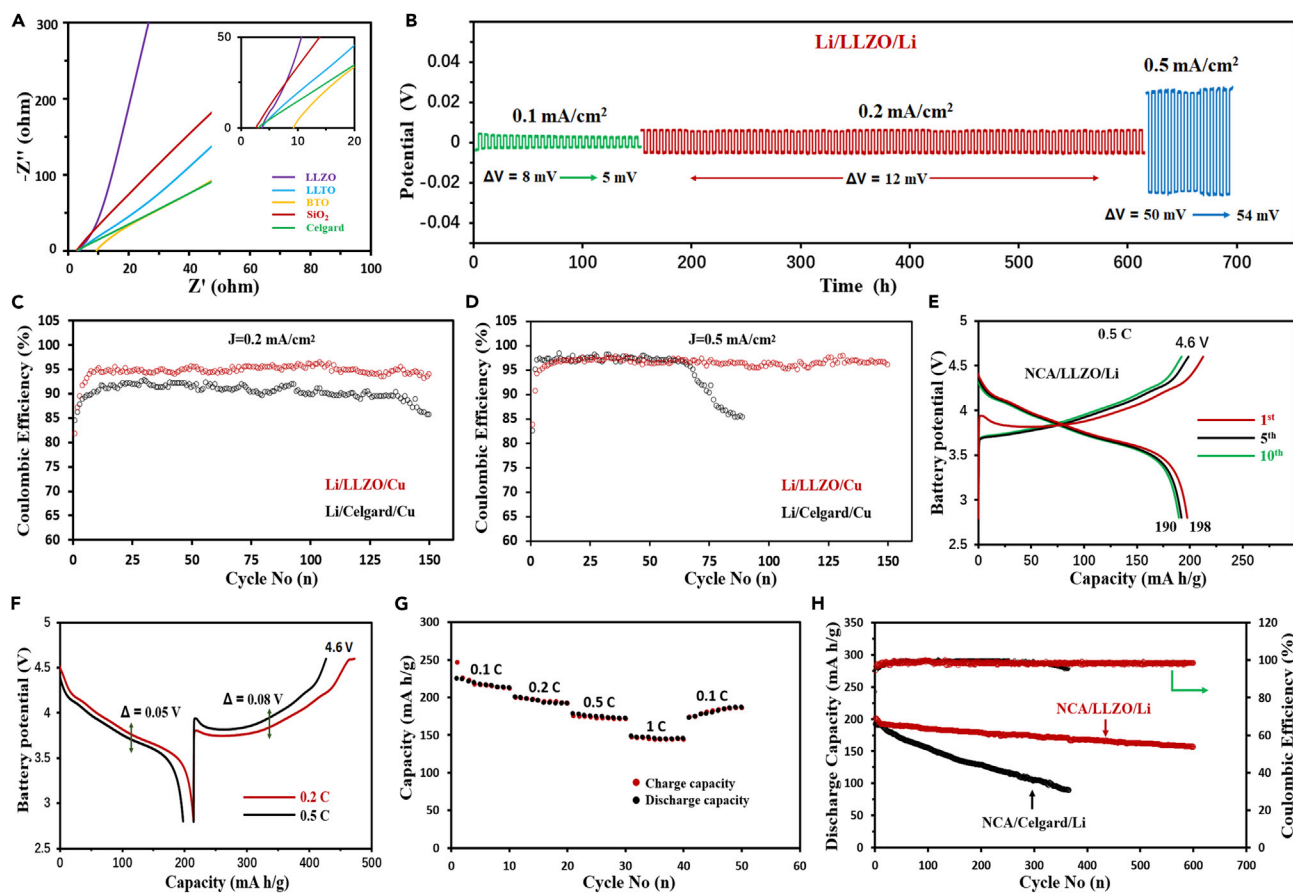
Figure 4. Electrochemical Characterizations and Tests

(A) Impedance spectra of the ceramic separators and the Celgard 2,500 separator.

(B–D) (B) Galvanostatic plating and striping measurements of Li||Li symmetric cells with different current densities at room temperature. Comparison of Columbic efficiency of Li||Cu asymmetric cells containing the LLZO ceramic NF separators and the Celgard 2,500 under a current density of (C) 0.2 mA/cm² and (D) 0.5 mA/cm².

(E) Galvanostatic charge-discharge profiles of NCA/LLZO/Li with a termination charging voltage of 4.6 V at 0.5 C.

(F) Voltage plateau gaps of NCA/LLZO/Li cells at 0.2 and 0.5 C.

(G) Rate capability of the NCA/LLZO/Li cells from 0.1 to 1 C.

(H) Long-term cycling tests of the NCA/Li cells with different separators at 0.5 C.

The battery of NCA//LLZO//Li exhibited typical voltage profiles with a low termination charging voltage of 4.3 V at various current rates ranging from 0.1 to 1 C (Figure S14). When promoting the charge termination voltage to 4.6 V, the batteries could run normally with enhanced discharge capacities, i.e., ~190 mA h/g at 0.5 C (Figure 4E) and ~210 mA h/g at 0.2 C (Figure S15). Of note, the voltage gaps at 0.5 and 0.2 C were only 50 mV (for discharge plateaus) and 80 mV (for charge plateaus) (Figure 4F), further verifying the small polarization of the ceramic LLZO separators. Interestingly, the capacity was almost fully recovered from 150 mA h/g to 180 mA h/g when the current rates were brought back from 1 C to the initial 0.1 C (Figure 4G), indicating a good rate capability of the LLZO ceramic separators. Accordingly, the ceramic-based batteries at 0.5 C rendered a capacity increase of ~60 mA h/g when compared with the Celgard 2,500-based batteries, and the capacity retention was also significantly improved over 600 cycles (Figure 4H), indicating high chemical stability of the ceramic separator without reacting with electrode materials and the liquid electrolytes at high voltage chemistry.

DISCUSSION

Oxide ceramics are commonly regarded as brittle materials. Although there have been several reports of single or organic crystals that exhibited plastic bending (Worthy et al., 2018; Panda et al., 2015), there were few reports about soft polycrystalline materials like multicomponent oxide ceramics. The

techniques used in this article were adaptations of electrospinning methods that had received considerable recent attention for making nanoscale fibers. The successful synthesis of soft oxide ceramics provided a robust methodology to explore the assembly of ceramic NFs and their applications in a 2D porous form with nanoarchitectures. Here, four selected polymers, from the binary oxides of SiO_2 to the complex ternary oxide of BTO and quaternary oxides of LLTO and LLZO, served as model systems for a proof of concept. In considering the ease of optimization of sol-gel electrospinning parameters and calcination processes, our findings provide a versatile platform for designing new types of soft ceramics.

Preparation of soft oxide ceramics while maintaining their robust strength to meet the practical applications has become an open problem. In this article, we showed that a nanofibrous structure constituted by densely arranged ceramic NPs exhibited the function of shape memory as well as robust elastic strength. As the breakages and cracks could easily occur at the boundary in the NFs, we tried to flatten the boundaries between the ceramic grains by employing polymer NFs as soft templates. It is worthy to note that to obtain the oxide ceramics, a low temperature of <900°C and a short calcination time of 3–7 h were applied, greatly reducing power energy consumption and time cost when compared with the traditional solid-phase sintering techniques that required a higher calcination temperature of >1,300°C and a longer calcination time of >24 h (Tang et al., 2017; Buschmann et al., 2011). We speculate that the nanofibrous structures facilitated the crystal transition at a lower temperature in a short time. These nanoscale ceramic particles tightly bonded with each other, and some of them even fused together to form common boundaries (Figure S16), enhancing the robustness and thus rendering the oxide ceramics with combined characteristics of softness and hardness.

To advance these soft and robust ceramic NF films into the applications of battery separators, the most essential properties that should be considered include weight density, impedances, and electrolyte uptake capability. The weight affects the battery energy density, whereas the other two have a great impact on battery reliability and safety, as well as performance and calendar lives. Electrospinning presents many advantages such as the ease of adjusting the morphology and compositions of fibers as well as the porosity and thickness of the films to achieve the desired functionalities, offering a wide diversity in designing soft ceramic forms (Si et al., 2014, 2016; Agarwal et al., 2013). Of note, the film thicknesses could be finely adjusted from several to hundreds of micrometers, as shown in Figure S17.

The pore sizes and the porosities of the electrospun ceramic films were closely related to the thicknesses of the films, as verified by the air permeability of the films with different thicknesses (Table S2). Specifically, the thin nature of the film resulted in a larger air permeability. Therefore to control the pore sizes, we adjusted the thicknesses of the ceramic films between 30 and 50 μm. In addition, when these ceramic films were applied as battery separators, to eliminate the possible macropores, we added 1.5 wt % polyvinylidene difluoride (PVDF) polymers in the liquid electrolytes to eliminate the possible macropores in the ceramic films and to further enhance the mechanical integrity of the ceramic separators. Figure S18 and Table S3 show the detailed information of the pore size and pore size distributions of these four types of ceramic NF separators. For example, the average pore size of the LLZO separators was as small as 0.19 μm, which was smaller than those of the commercial electrospun battery separators, showing a great potential to apply them into battery separators.

Combining these merits together, the NCA//LLZO//Li batteries with a high voltage chemistry (i.e., 4.6 V) exhibited enhanced cycling stability with minimum "dead or dendrite Li" moieties after 500 cycles at 0.5 C (Figure S19). Such chemical, mechanical, and thermal responses of these soft ceramic separators make it possible to construct reliable and safe batteries with Li metal as anodes and high-voltage NCA materials as cathodes even at a high temperature of 100°C (Figure S20) without thermal runaway. All these results indicated the potential applications of such novel ceramic separators in advanced Li-batteries. The ceramic separator displayed better thermal stability and durability when compared with recently reported ultrastrong separators or ionic conductor separators (Tung et al., 2015; Jiang et al., 2013; Lin et al., 2016). We believe this finding will have a great impact on the general approaches of achieving soft oxide ceramics with controllable morphology and thickness. In addition, soft ceramic materials like these could enable the design of a range of new hybrid materials that fall between the boundaries of what have typically been regarded as the limitations of hard and soft matter.

Conclusion

We have developed a technique of sol-gel electrospinning followed by calcination that can be broadly applied for the fabrication of soft, light, and robust oxide ceramic NF films. A series of soft oxide ceramics from binary oxide of SiO_2 to multicomponent oxides of BTO, LLTO, and LLZO were created. The optimum conditions for forming these oxide ceramic NFs were established, and the deformation mechanisms between the polycrystals and grains during the bending of a single NF and an NF film were also explored. When applying these ceramic films in Li-batteries, they exhibited low internal ionic penetration resistivity, high chemical stability, and robust mechanical strength, enabling a stable Li plating-stripping cycling with high efficiency and an enhanced long-term stability of NCA//Li cells at a high voltage chemistry of 4.6 V. More importantly, such ceramic NF separators rendered the batteries with a high thermal stability over the operating temperature ranges without thermal runaway. This work provides a promising strategy to produce oxide ceramic films that possess both soft and rigid properties with a low-cost and scalable synthesis method.

Limitation of the Study

Our preliminary results show that the soft ceramic NF films with controllable morphology and thickness could be fabricated by adjusting the parameters of electrospinning and calcination. Although we demonstrated the potential applications of these ceramic NF films as battery separators, if the following two technical problems can be addressed, the reliability of such separators will be significantly enhanced. (1) During our preliminary research, we tried to minimize the pore sizes of the ceramic separators by increasing the thickness of the films and by adding a small amount of PVDF polymers in the electrolytes. In spite of this, the films still had a larger average pore size than the commercial separators. The larger thickness of the ceramic separators may cause a low volumetric energy density, while its large pore sizes may facilitate Li-dendrite growth along the pores. (2) In this study, we tested the performance of the ceramic separators by constructing half-cells with Li metal as anode and using limited liquid electrolytes, which we called hybrid-solid separator. However, we did not characterize the ability of such ceramic separators to resist the Li dendrite growth, which was also an unsafety factor.

METHODS

All methods can be found in the accompanying Transparent Methods supplemental file.

SUPPLEMENTAL INFORMATION

Supplemental Information can be found online at https://doi.org/10.1016/j.isci.2019.04.028.

AUTHOR CONTRIBUTIONS

J.Y. and B.D. conceived and designed the experiments. Y.Zhao, S.X., X.W., Y.H., and Y.Zhang synthesized the ceramic NFs. Y.Zhao, S.X., and X.W. conducted material characterizations. J.Y. and Y.Zhao conducted battery tests and analysis. J.Y. wrote this paper, and all authors contributed to discussing and revising the paper.

DECLARATION OF INTERESTS

The authors declare no competing interests.

REFERENCES

Agarwal, S., Greiner, A., and Wendorff, J. (2013). Functional materials by electrospinning of polymers. Prog. Polym. Sci. *38*, 963–991.

Belmonte, M. (2006). Advanced ceramic materials for high temperature applications. Adv. Eng. Mater. *8*, 693–703.

Buschmann, H., Dolle, J., Berendts, S., Kuhn, A., Bottke, P., Wilkening, M., Heitjans, P., Senyshyn, A., Ehrenberg, H., Lotnyk, A., et al. (2011). Structure and dynamics of the fast lithium ion conductor "$Li_7La_3Zr_2O_{12}$". Phys. Chem. Chem. Phys. *13*, 19378–19392.

Cai, Y., Song, J., Liu, X., Yin, X., Li, X., Yu, J., and Ding, B. (2018). Soft $BiOBr@TiO_2$ nanofibrous membranes with hierarchical heterostructures as efficient and recyclable visible-light photocatalysts. Environ. Sci.Nano *5*, 2631–2640.

Cho, J., Jung, Y., Lee, Y., and Kim, D. (2017). High performance separator coated with amino-functionalized SiO_2 particles for safety enhanced lithium-ion batteries. J. Membr. Sci. *535*, 151–157.

Costa, C.M., Nunes-Pereira, J., Rodrigues, L.C., Silva, M.M., Gomez Ribelles, J.L., and Lanceros-Méndez, S. (2013). Novel poly(vinylidene fluoride-trifluoroethylene)/poly(ethylene oxide) blends for battery separators in lithium-ion applications. Electrochim. Acta *88*, 473–476.

Dai, J., Shi, C., Li, C., Shen, X., Peng, L., Wu, D., Sun, D., Zhang, P., and Zhao, J. (2016). A rational design of separator with substantially enhanced thermal features for lithium-ion batteries by the polydopamine-ceramic composite modification of polyolefin membranes. Energ. Environ. Sci. *9*, 3252–3261.

Ge, J., Qu, Y., Cao, L., Wang, F., Dou, L., Yu, J., and Ding, B. (2016). Polybenzoxazine-based highly porous carbon nanofibrous membranes hybridized by tin oxides nanoclusters: durable mechanical elasticity and capacitive performance. J. Mater. Chem. A *4*, 7795–7804.

Han, W., Ding, B., Park, M., Cui, F., Chae, S., and Kim, H. (2016). Insight into the precursor nanofibers on the flexibility of La_2O_3-ZrO_2 nanofibrous membranes. E Polymer. *17*, 243–248.

Han, W., Cui, F., Si, Y., Mao, X., Ding, B., and Kim, H. (2018). Self-assembly of perovskite crystals anchored Al_2O_3-La_2O_3 nanofibrous membranes with robust flexibility and luminescence. Small *14*, 1801963.

Jiang, W., Liu, Z., Kong, Q., Yao, J., Zhang, C., Han, P., and Cui, G. (2013). A high temperature operating nanofibrous polyimide separator in Li-ion battery,. Solid State Ionics *232*, 44–48.

Kim, K.M., Park, N.G., Ryu, K.S., and Chang, S.H. (2006). Characteristics of PVdF-HFP/TiO_2 composite membrane electrolytes prepared by phase inversion and conventional casting methods. Electrochim. Acta *51*, 5636–5644.

Kim, J., Gu, M., Lee, D., Kim, J., Oh, Y., Min, S., Kim, B., and Lee, S. (2016). Functionalized nanocellulose-integrated heterolayered nanomats toward smart battery separators. Nano Lett. *16*, 5533–5541.

Lee, T., Kim, W., Lee, Y., Ryou, M., and Lee, Y. (2014). Effect of Al_2O_3 coatings prepared by RF sputtering on polyethylene separators for high-power lithium ion batteries. Macromol. Res. *22*, 1190–1195.

Liao, H., Hong, H., Zhang, H., and Li, Z. (2016). Preparation of hydrophilic polyethylene-methylcellulose blend microporous membranes for separator of lithium-ion batteries. J. Membr. Sci. *498*, 147–157.

Lin, D., Zhuo, D., Liu, Y., and Cui, Y. (2016). All-Integrated bifunctional separator for Li dendrite detection via novel solution synthesis of a thermostable polyimide separator. J. Am. Chem. Soc. *138*, 11044–11050.

Liu, K., Zhuo, D., Lee, H., Liu, W., Lin, D., Lu, Y., and Cui, Y. (2017). Extending the life of lithium-based rechargeable batteries by reaction of lithium dendrites with a novel silica nanoparticle sandwiched separator. Adv. Mater. *29*, 1603987.

Nunes, P.J., Costa, C.M., and Lanceros, M.S. (2015). Polymer composites and blends for battery separators: state of the art, challenges and future trends. J. Power Sources *281*, 378–398.

Pan, Y., Chou, S., Liu, H., and Dou, S. (2017). Functional membrane separators for next-generation high-energy rechargeable batteries. Nat. Sci. Rev. *6*, 917–933.

Panda, M., Ghosh, S., Yasuda, N., Moriwaki, T., Mukherjee, G., Reddy, C., and Naumov, P. (2015). Spatially resolved analysis of short-range structure perturbations in a plastically bent molecular crystal. Nat. Chem. *7*, 65–72.

Prosini, P.P., Villano, P., and Carewska, M. (2002). A novel intrinsically porous separator for self-standing lithium-ion batteries. Electrochim. Acta *48*, 227–233.

Qian, J., Henderson, W., Xu, W., Bhattacharya, P., Engelhard, M., Borodin, O., and Zhang, J. (2015). High rate and stable cycling of lithium metal anode. Nat. Commun. *6*, 6362–6370.

Shi, C., Zhang, P., Huang, S., He, X., Yang, P., Wu, D., Sun, D., and Zhao, J. (2015). Functional separator consisted of polyimide nonwoven fabrics and polyethylene coating layer for lithium-ion batteries. J. Power Sources *298*, 158–165.

Si, Y., Yu, J., Tang, X., Ge, J., and Ding, B. (2014). Ultralight nanofibre-assembled cellular aerogels with superelasticity and multifunctionality. Nat. Commun. *5*, 5802.

Si, Y., Wang, X., Yan, C., Yang, L., Yu, J., and Ding, B. (2016). Ultralight biomass-derived carbonaceous nanofibrous aerogels with superelasticity and high pressure-sensitivity. Adv. Mater. *28*, 9512–9518.

Song, D., Xu, C., Chen, Y., He, J., Zhao, Y., Li, P., Lin, W., and Fu, F. (2015). Enhanced thermal and electrochemical properties of PVDF-HFP/PMMA polymer electrolyte by TiO_2 nanoparticles. Solid State Ionics *282*, 31–36.

Tang, Y., Zhang, Q., Luo, Z., Liu, P., and Lu, A. (2017). Effects of Li_2O-Al_2O_3-SiO_2, system glass on the microstructure and ionic conductivity of $Li_7La_3Zr_2O_{12}$ solid electrolyte. Mater. Lett. *193*, 251–254.

Tarascon, J., and Armand, M. (2001). Issues and challenges facing rechargeable lithium batteries. Nature *414*, 359–367.

Tung, S., Ho, S., Yang, M., Zhang, R., and Kotov, N. (2015). A dendrite-suppressing composite ion conductor from aramid nanofibers. Nat. Commun. *6*, 6152.

Wang, M., Chen, X., Wang, H., Wu, H., Jin, X., and Huang, C. (2016). Improved performances of lithium-ion batteries with a separator based on inorganic fibers. J. Mater. Chem. A *1*, 311–318.

Wang, Z., Pan, R., Ruan, C., Edström, K., Strømme, M., and Nyholm, L. (2018). Redox-active separators for lithium-ion batteries. Adv. Sci. *5*, 1700663.

Worthy, A., Grosjean, A., Pfrunder, M., Xu, Y., Yan, C., Edwards, G., Clegg, J., and McMurtrie, J. (2018). Atomic resolution of structural changes in elastic crystals of copper(II) acetylacetonate. Nat. Chem. *10*, 65–69.

Wu, J., Fan, Z., Xiao, D., Zhu, J., and Wang, J. (2016). Multiferroic Bismuth ferrite-based materials for multifunctional applications: ceramic bulks, thin films and nanostructures. Prog. Mater. Sci. *84*, 335–402.

Xiang, H., Chen, J., Li, Z., and Wang, H. (2011). An inorganic membrane as a separator for lithium-ion battery. J. Power Sources *196*, 8651–8655.

Xiao, W., Wang, Z., Zhang, Y., Fang, R., Yuan, Z., Miao, C., Yan, X., and Jiang, Y. (2018). Enhanced performance of P(VDF-HFP)-based composite polymer electrolytes doped with organic-inorganic hybrid particles PMMA-ZrO_2 for lithium ion batteries. J. Power Sources *382*, 128–134.

Yanilmaz, M., Lu, Y., Zhu, J., and Zhang, X. (2016). Silica/polyacrylonitrile hybrid nanofiber membrane separators via sol-gel and electrospinning techniques for lithium-ion batteries. J. Power Sources *313*, 205–212.

Yu, J., Kwon, H., Lee, W., Kim, K., and Park, M. (2014). Ceramic composite separators coated with moisturized ZrO_2 nanoparticles for improving the electrochemical performance and thermal stability of lithium ion batteries. Phys. Chem. Chem. Phys. *16*, 9337–9343.

Zhang, H., Liao, X., Guan, Y., Xiang, Y., Li, M., Zhang, W., Zhu, X., Ming, H., Lu, L., Qiu, J., et al. (2018). Lithiophilic-lithiophobic gradient interfacial layer for a highly stable lithium metal anode. Nat. Commun. *9*, 3729.

Supplemental Information

Polymer Template Synthesis

of Soft, Light, and Robust Oxide

Ceramic Films

Jianhua Yan, Yun Zhao, Xiao Wang, Shuhui Xia, Yuanyuan Zhang, Yuhui Han, Jianyong Yu, and Bin Ding

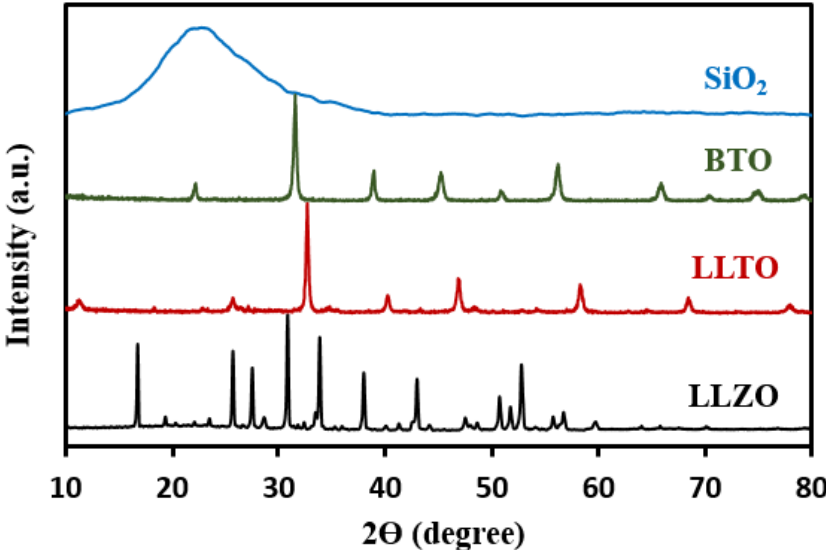## Supplementary Figures

Figure S1. XRD speactra of the five types of ceramic NF materials, related to Figure 1(b). The results indicated that the LLZO had a standard garnet type structure, the LLTO and BTO had perovskite structures, the ZrO_2 had a tetragonal structure, while the SiO_2 had an amorphous structure.
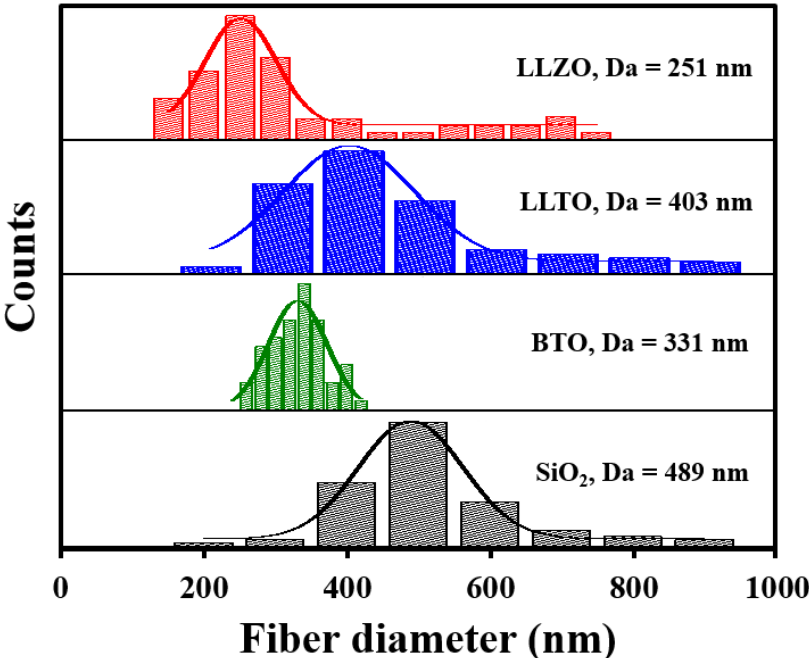
Figure S2. The ceramic NF diameter histograms, related to Figure 1(b). The average NF diameters of LLZO, LLTO, BTO, ZrO_2 and SiO_2 were 251 nm, 403 nm, 331 nm, 489 nm and 282 nm, respectively. BTO had smaller diameter range in comparsion with LLZO, LLTO and SiO_2.

1
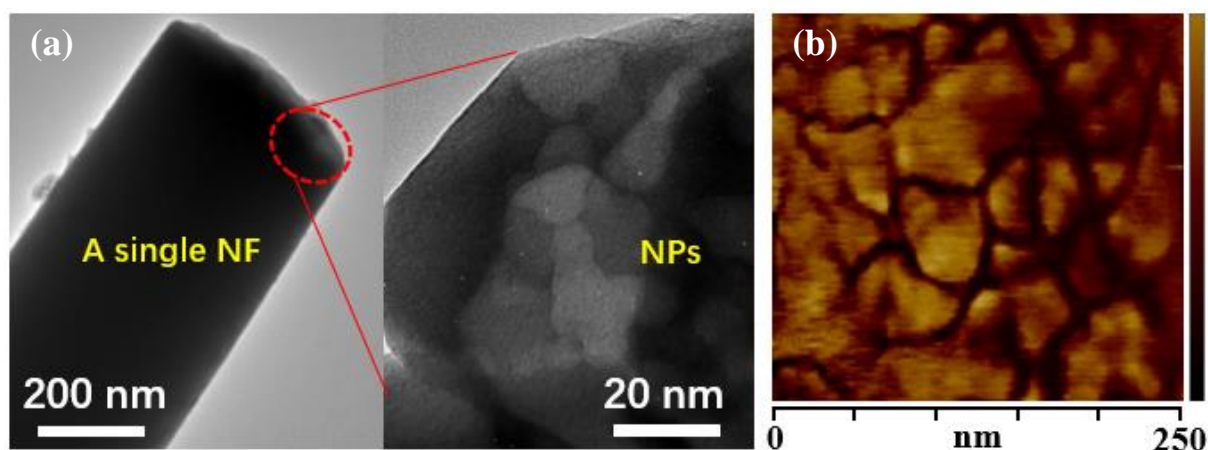
Figure S3. TEM and AFM characterizations of the ceramic NFs, related to Figure 1(b).
(a) A single ceramic NF that contained primary nanoscale grains, which were bonded with each other to form secondary NPs. (b) AFM characterization of a cross-sectional morphology of a ceramic NF, which showed the distributions of the ceramics NPs.
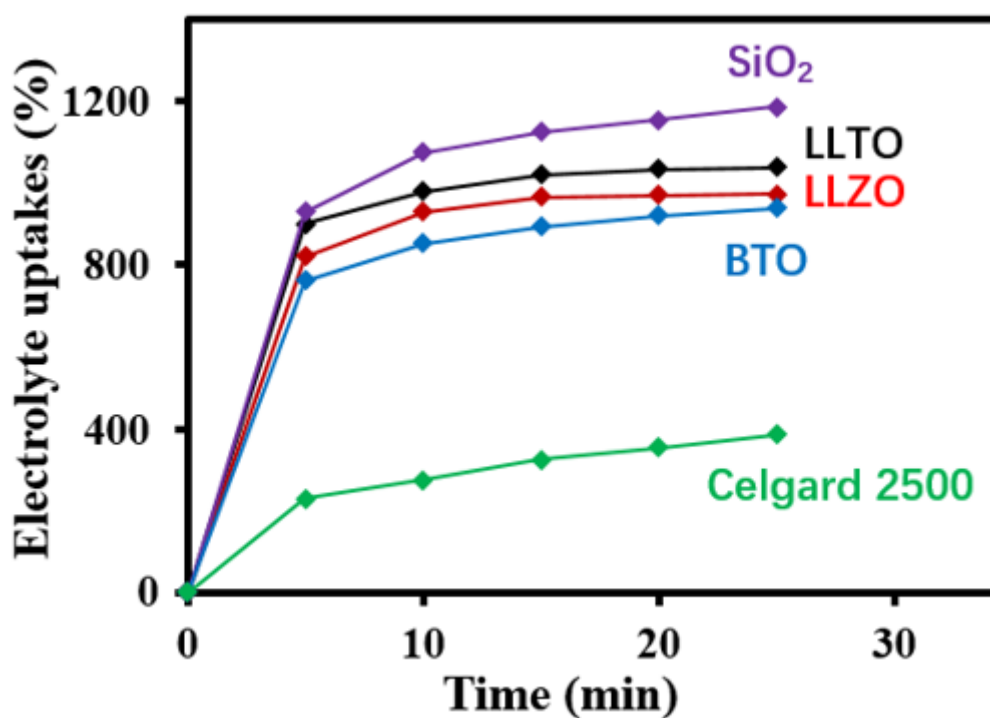
Figure S4. Electrolyte uptakes of the ceramic NF films and the Celgard 2500, related to Figure 1(c).
All the ceramic NF membranes exhibited markedly enhanced electrolyte wettability in comparison with the Celagard, and delivered ultra-large electrolyte uptakes of > 900%.
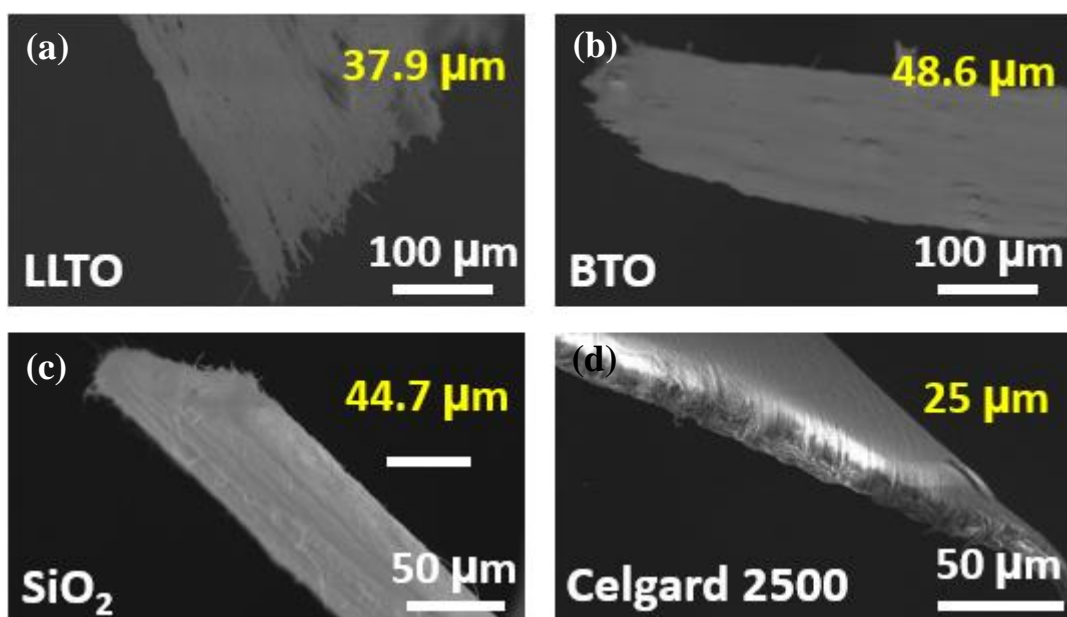
Figure S5. The cross-sectional SEM images of the ceramic NF films and the Celgard 2500, related to Figure 2(a).

The thickness of LLTO, BTO, SiO$_2$ and the Celgard were 37.9 μm, 48.6 μm, 44.7 μm and 25 μm, respectively.

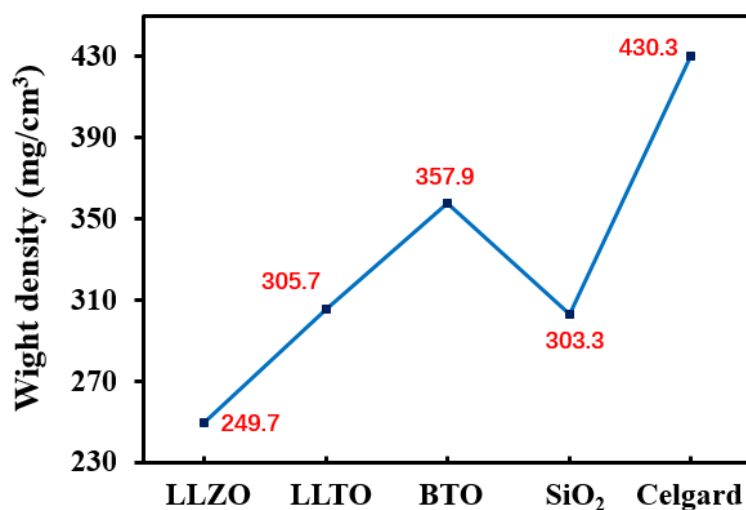**Figure S6. A large-scale ceramic NF membrane with an area of 12000 cm^2, related to Figure 2(a).**

Figure S7. The bulk weight density of the ceramic NF films and the Celgard 2500, related to Figure 2(h).

The bulk weight density was calculated according to $B_d = \frac{m}{S \times d}$, where m was the weight as shown in Fig. S8, the S and d were the areas and thickness of the membranes, as shown in Tab. S1.
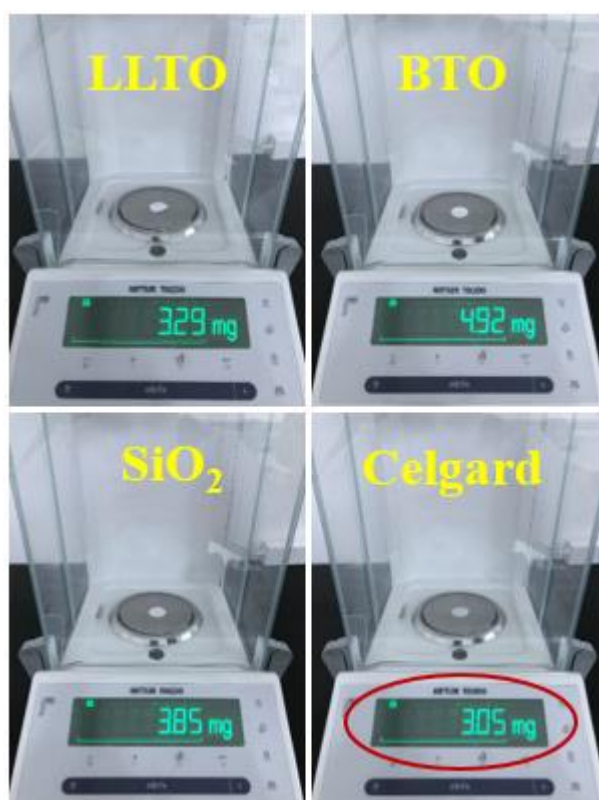
Figure S8. The weights of the ceramic NF films and the Celgard 2500, related to Figure 2(h).

The diameter of the cicular separator was 19 mm, corresponding to an area of 2.84 cm$^{2.}$ The thicknesses of these separators were shown in Tab. S1.
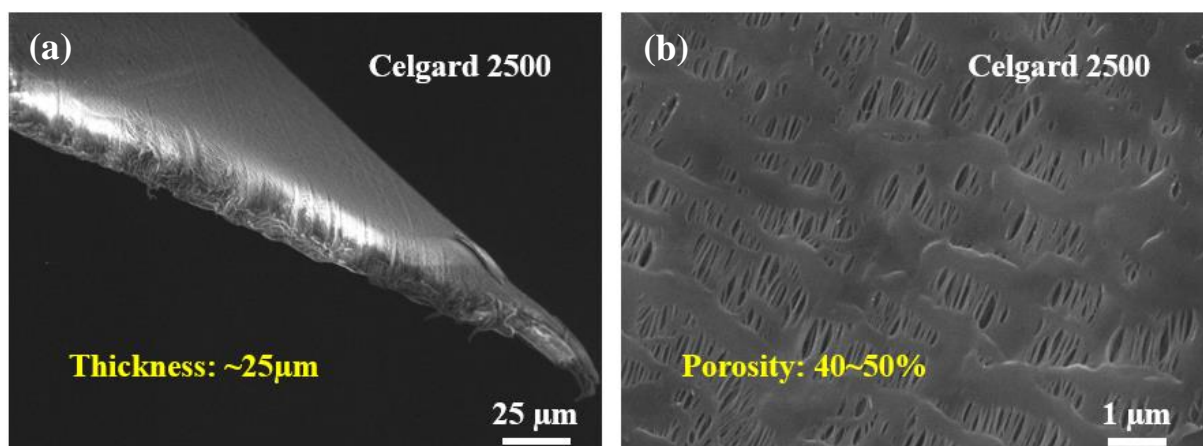
Figure S9. SEM images of the Celgard 2500 separators under (a) low and (b) high magnifications, related to Figure 2(h).

The separator had a thickness of about 25 μm and a porosity of 40~50%.
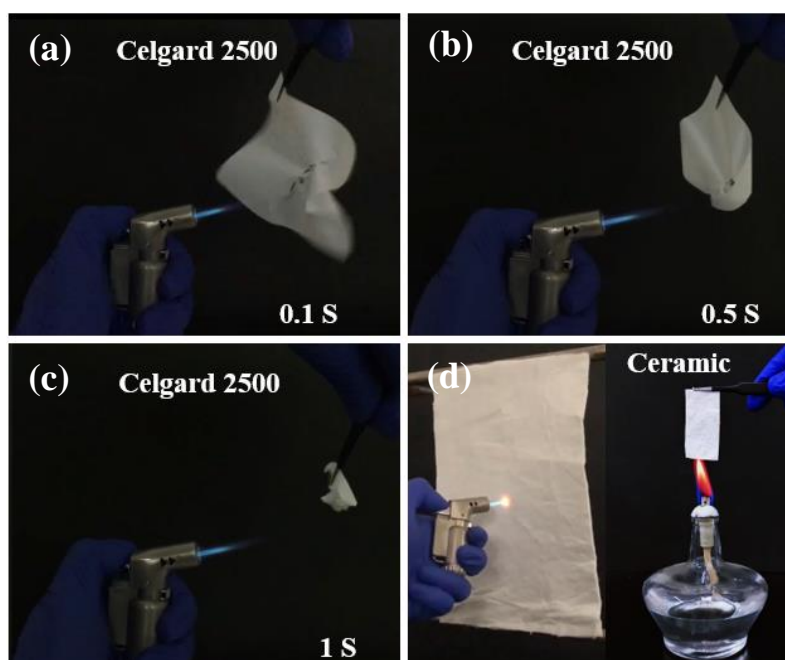

Figure S10. Comparison of the thermal resistances between the Celgard 2500 and the ceramic films, related to Figure 2(i).

(a-c) A continuous process shows the inferior thermal stability of the Celgard 2500 separator in comparison with (d) the ceramic NF films, which were stable without shrinkage when being heated by an alcohol lamp and a butane blowtorch.
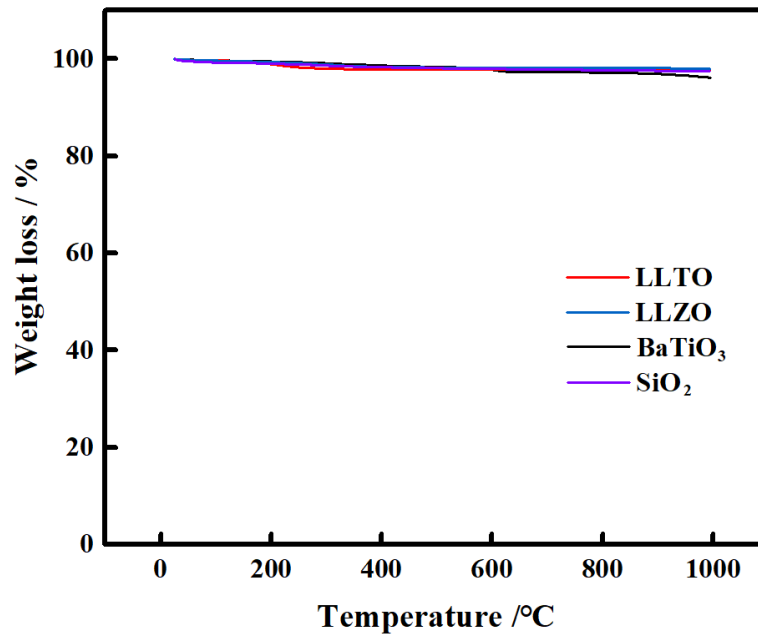
Figure S11. TGA curves of the five types of ceramic NFs, related to Figure 2(i).

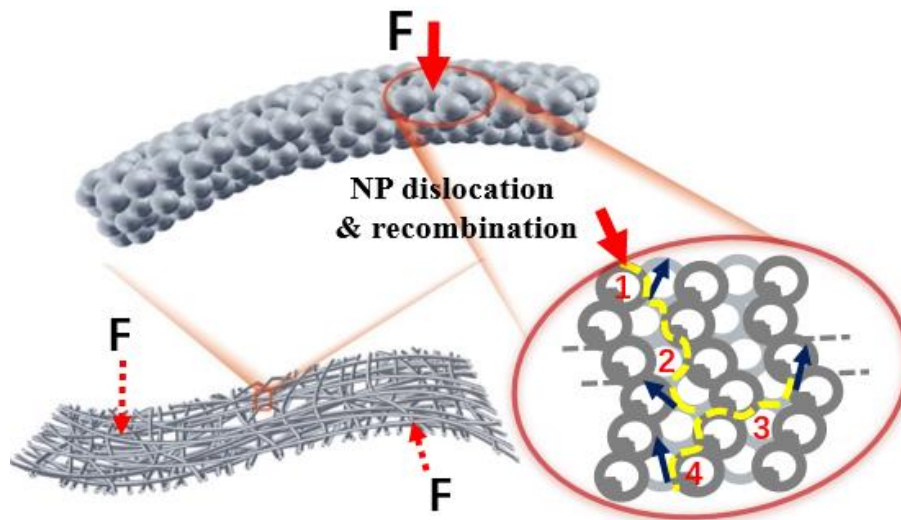These NF materials were stable over the entire testing period from room temperature to 1000 °C without degradations.

Figure S12. A sketch of a single ceramic NF under an external bending force, related to Figure 3(e-g).

The ceramic NPs could scatter the concentrated force by dislocations and recombinations as indicated by the movements of NPs 1-4.
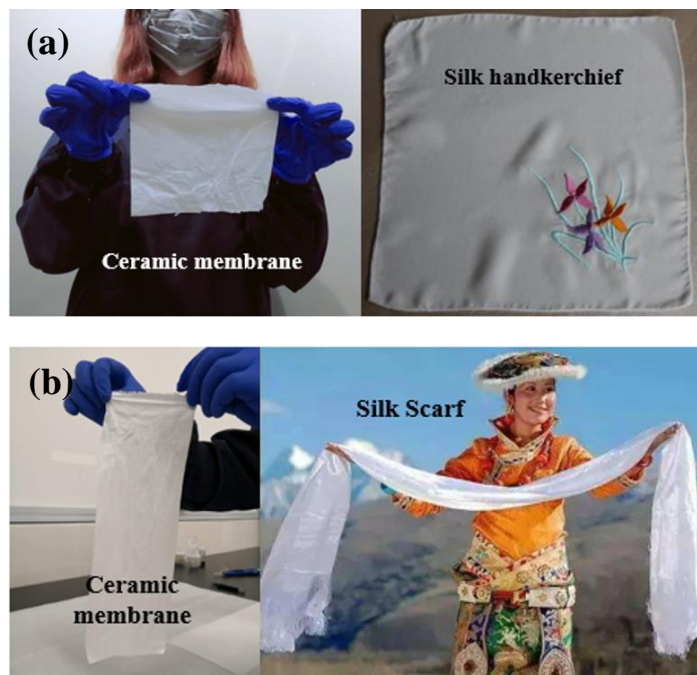
Figure S13. **An intuitive comparison between the fabricated ceramic NF films and a silk handkerchief ora silk scarf, related to Figure 3(e-g).**

The ceramic NFs did not possess the property of elastic bending, but exhibited a soft property like silk.
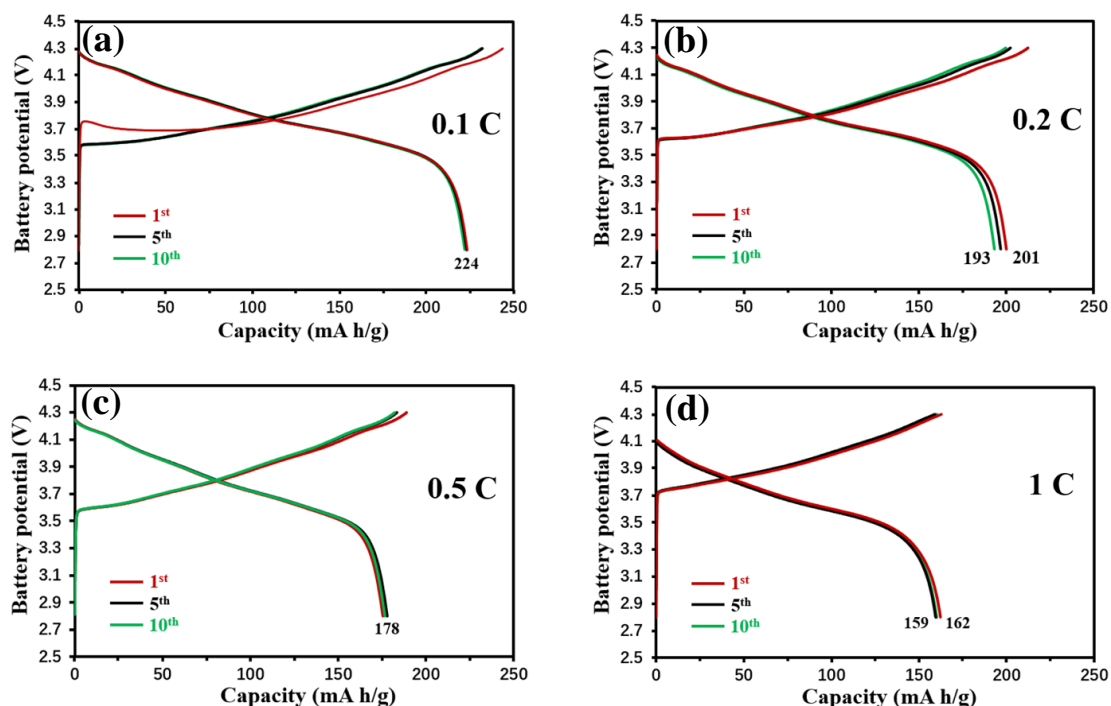

Figure S14. Galvanostatic charge-discharge profiles of NCA/LLZO/Li with a termination charging voltage of 4.3 V, related to Figure 4(c-d).

All these batteries at different current rates of (a) 0.1 C, (b) 0.2 C, (c) 0.5 C and (d) 1 C demonstrated typical voltage profiles of NCA in a liquid-type battery.
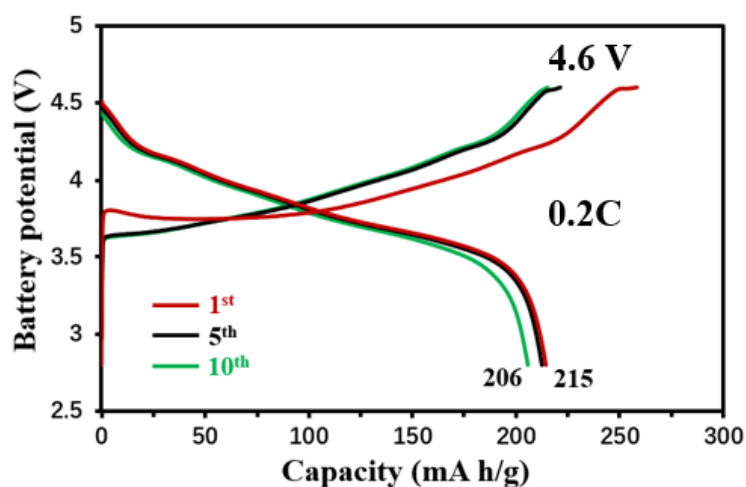
Figure S15. **Galvanostatic charge-discharge profiles of NCA/LLZO/Li with a termination charging voltage of 4.6 V at 0.2 C, related to Figure 4(e).**
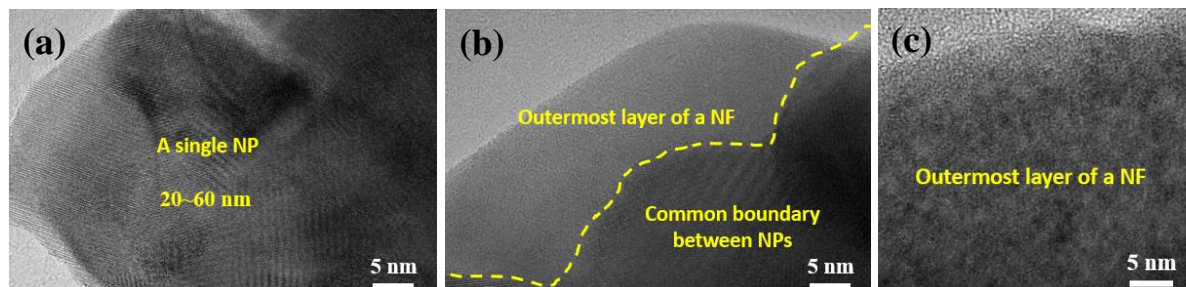

Figure S16. A group of TEM figures that exhibited the common boundaries between the adjacent NPs, related to Figure 4(e-g).

These nanoscale ceramic particles tightly bonded with each other and some of them even fused together to form common boundaries, enhancing the robustness of the polycrystalline ceramics.
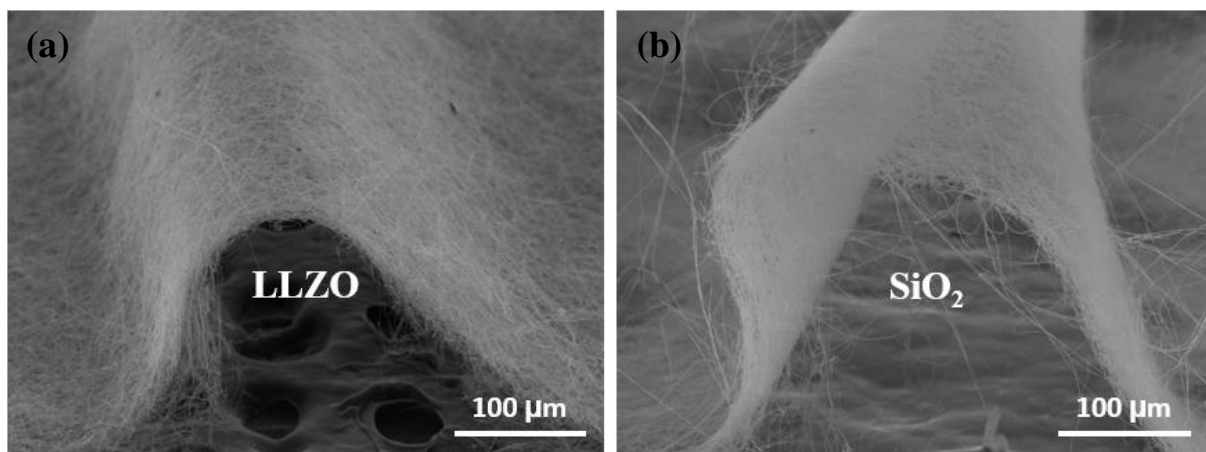
Figure S17. SEM figures of ultrathin ceramic NF films, related to Figure 2(f).
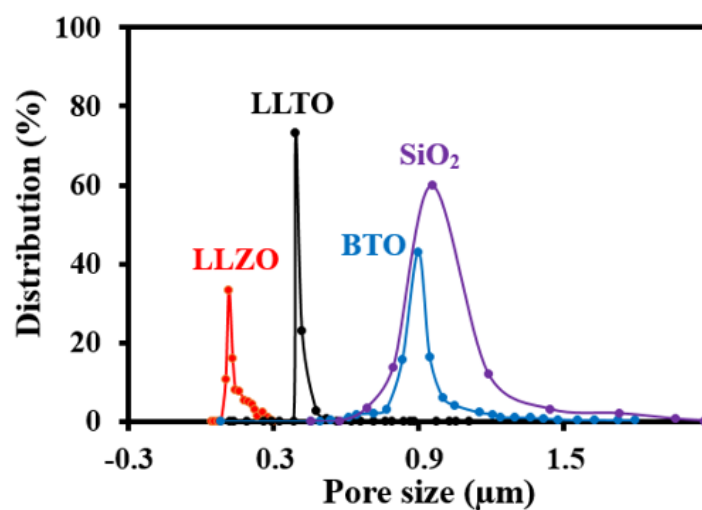(**a**) LLZO and (**b**) SiO$_2$ films.

Figure S18. Pore-size analysis of the fabricated hybrid-solid ceramic NF electrolytes, related to Figure 2(g).

The pore-sizes were tested with a PMI machine. The detailed information about the pore-sizes were summarized in Tab. S2.

9
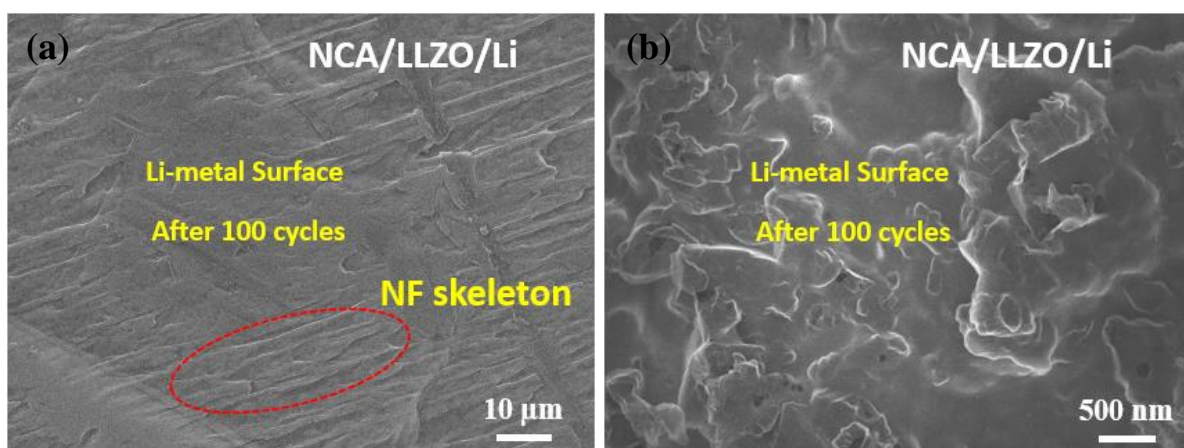
Figure S19. The surface morphology of the Li-metal anodes after 100 cycles in the NCA/LLZO/Li batteries, related to Figure 4(b).

The batteries were tested with a high voltage chemistry (i.e. 4.6 V) and a lean electrolyte (4 ml/g) at 0.5 C. There were no obvious Li-dendrites, indicating a conformal Li-deposion.
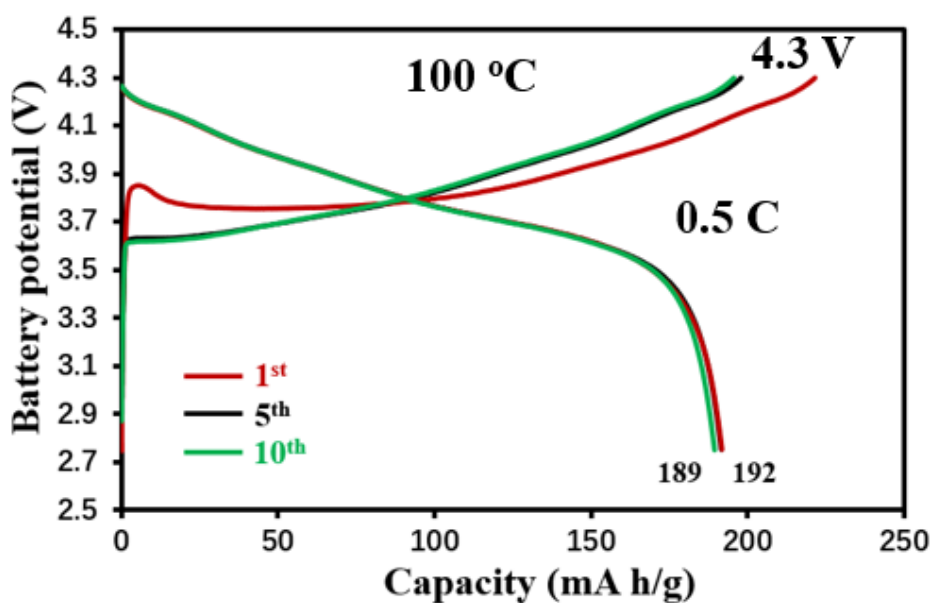
Figure S20. Galvanostatic charge-discharge profiles of NCA/LLZO/Li with a termination charging voltage of 4.3V at 0.5 C, related to Figure 4(h).

The testing temerature was 100 ℃.

Supplementary Tables

Table S1. The detailed information of the bulk resistances, sizes and ionic conductivities of the ceramic NF separators and the commercial Celgard 2500 separator, related to Figure S7.

|	LLZO	LLTO	BTO	SiO$_2$	Celgard
R$_b$ (Ω)	3.775	3.661	9.306	2.722	2.28
S (cm^2)	2.84	2.84	2.84	2.84	2.84
d (cm)	39.2×10^{-4}	37.9×10^{-4}	48.4×10^{-4}	44.7×10^{-4}	25×10^{-4}
σ(ms/cm)	0.366	0.364	0.183	0.578	0.386

Table S2. The detailed information about the air permeability (cm^3/cm$^2\cdot$S) of the ceramic LLZO NF films, related to Figure S17.

The air pressure was set as 200 Pa, and we tested 8 times for each sample. The thicknesses of the three samples were 41, 61 and 85 μm, respectively.

Samples	1st	2nd	3rd	4th	5th	6th	7th	8th	average
Sample 1 (41 μm)	4.8	5.3	4.9	5	4.9	4.7	4.9	4.9	4.93
Sample 2 (61 μm)	4.1	4	3.9	4.2	4.1	4.3	4.1	4.1	4.1
Sample 3 (85 μm)	3.3	3.8	3.3	3.7	3.6	3.7	3.6	3.7	3.59

Table S3. The detailed information about the pore-sizes and their distributions in the ceramic NF membranes, related to Table S18. The pore-sizes were checked by porosity analysis meter (PMI model).

	LLZO	LLTO	BTO	SiO$_2$
Optimal pore-size (µm) and distribution (%)	0.19	0.65	1.5	1.6
	33.5%	73.5%	42.9%	59.9%
Pore size (µm) range (smallest-biggest)	0.138	0.762	1.19	1.14
	0.762	0.959	2.16	3.47

Transparent Methods

Material Synthesis

Synthesis of LLZO NFs. Unless otherwise specified, all chemical were obtained from Aladdin with a purity of 95% or higher. First, a PVP (1,300,000) solution was prepared by dissoving the PVP into deionized water with a concentration of 6.5 wt.% and then were stirred for 3 h to prepare clean solution. Then, stoichiometric amounts of LiNO$_3$, La(NO$_3$)$_3$ 6H$_2$O and C$_8$H$_{12}$O$_8$Zr (solution, weight percent of 15.0~16.0 %) were successively added into ethanol and then were stirred for 2 h to prepare the salt gel. Second, the PVP solution and the salt gel were mixed together and were stirred for 1 h to prepare the sol-gel precursor solution. The salts and the PVP were mixed at a ratio of 1:4.4 in weight. Of note, an additional 10 wt.% of LiNO$_3$ was added to compensate for the Li-loss during the calcination at high temperatures. Third, the electrospinning process was carried out with a feed rate of 1.5 mL/h, a voltage of 15 kV and a distance of 15 cm between the nozzle and the collector. The rotation speed was controlled as 60 r/m. The humidity and temperature of the electrospinning chamber were 45% ±5% and 25 ± 2℃, respectively. After electrospinning, the polymer NF precursors were kept in a vacuum oven at 60 ℃ for 2 h and then were successively calcined at 400 ℃ in air for 4 h and then 800 ℃ in air for 4 h at a heating rate of 2 ℃ min^{-1}. The detailed methods for synthesizing the ceramic NFs of LLTO, BTO and SiO$_2$ are summaried in the supplementary information.

Synthesis of LLTO NFs. Unless otherwise specified, all chemical were obtained from Aladdin with a purity of 95% or higher. First, a PVP (1,300,000) solution was prepared by dissoving the PVP into deionized water with a concentration of 7 wt.% and then were stirred for 3 h. Then, stoichiometric amounts of $C_{12}H_{28}O_4Ti$, $La(NO_3)_3 \cdot 6H_2O$ and $LiNO_3$ were successively added into a mixed solution of ethanol and Acetic acid (a weight ratio of 4:1) and were stirred at room temperature for 12 h to prepare the salt gel. Second, the PVP solution and the salt gel were mixed together and were stirred for 3 h. The salts and the PVP were mixed at a ratio of 1:4.8 in weight. Of note, an additional 10 wt.% of $LiNO_3$ was added to compensate for the Li-loss during the calcination at high temperatures. Third, the electrospinning process was carried out with a feed rate of 1.5 mL/h, a voltage of 15 kV and a distance of 20 cm between the nozzle and the collector. The rotation speed was controlled as 60 r/m. The humidity and temperature of the electrospinning chamber were 45% ± 5% and 25 ± 2°C, respectively. After electrospinning, the polymer NF precursors were kept in a vacuum oven at 60 °C for 2 h and then were successively calcined at 400 °C in air for 4 h and then 800 °C in air for 4 h at a heating rate of 2 °C min^{-1}.

Synthesis of BTO NFs. First, a PVP (1,300,000) solution was prepared by dissoving the PVP into deionized water with a concentration of 5 wt.% and then were stirred for 3 h. Then, stoichiometric amounts of Tetrabutyl titanate and $Ba(CH_3COO)_2$ were successively added into a mixed solution of deionized water, acetic acid and Ethanol (a weight ratio of 1:4:5) and were stirred at room temperature for 2 h to prepare the salt gel. Second, the PVP solution and the salt gel were mixed together and were stirred for 30 min. The salts and the PVP were mixed at a ratio of 1:20 in weight. Of note, an additional 10 wt.% of $LiNO_3$ was added to compensate for the Li-loss during the calcination at high temperatures. Third, the electrospinning process was carried out with a feed rate of 1.5 mL/h, a voltage of 15 kV and a distance of 15 cm between the nozzle and the collector. The rotation speed was controlled as 50 r/m. The humidity and temperature of the electrospinning chamber were 45% ± 5% and 25 ± 2°C, respectively. After electrospinning, the polymer NF precursors were kept in a vacuum oven at 80 °C for 2 h and then were successively calcined at 400 °C in air for 3 h and then 850 °C in air for 3 h at a heating rate of 2 °C min^{-1}.

Synthesis of SiO2 NFs. First, PVA (86,000) was dissolved in deionized water with a concentration of 10 wt.% and were stirred at 80 °C for 4 h. Then, tetraethyl orthosilicate, H_3PO_4 and H_2O were mixed at a molar ratio of 1:0.01:11 and were stirred at room temperature for 12 h to prepare the silica gel. Second, the silica gel and PVA solution were mixed at a weight ratio of 1:1 and were stirred for 4 h. Third, the electrospinning process was carried out with a feed

rate of 1.5 mL/h, a voltage of 20 kV and a distance of 15 cm between the nozzle and the collector. The rotation speed was controlled as 60 r/m. The humidity and temperature of the electrospinning chamber were 45% ±5% and 25 ±2 ℃, respectively. After electrospinning, the polymer NF precursors were kept in a vacuum oven at 80 ℃ for 2 h and then were calcined at 850 ℃ in air for 2 h at a heating rate of 5 ℃ min^{-1}.

Material Characterization

Morphology of the ceramic NFs were checked by SEM (Hitachi S-4800), TEM (JEM-2100F) and AFM (Veeco Dimension D3100). The crystal structures were tested using Bruker XRD with Cu Kα radiation between 10° and 80°. The TGA was conducted with air flowing atmosphere ramped from room temperature to 1000 ℃ at a scanning rate of 10 ℃ min^{-1} with SDT Q600. The softness of the ceramic membranes and the Celgard 2500 was recorded by a RRY-1000 softness tester at room temperature. The tensile properties were investigated by a XQ-1A testing machine (China) at a stretching speed of 5 mm/min. The thickness of the ceramic membranes was measured by a thickness gauge (CHY-C2, China).

Battery assemble and electrochemical characterizations.

The $LiNi_{0.8}Co_{0.15}Al_{0.05}O_2$ (NCA) cathdoes were prepared by mixing 80 wt.% of the NCA with 10 wt.% of PVDF and 10 wt.% of carbon black in an N-methyl- pyrrolidone (NMP) solution. The slurry was doctor bladed onto an aluminium foil and dried overnight at 80 ℃ under vacuum. The typical NCA loading was 3.5-4 mg/cm^2. Cathode disks with an area of 1.6 cm^2 were assembled into 2032-type coin cells. 1M $LiPF_6$ in diethyl carbonate, ethylmethyl carbonate and ethylene carbonate (DEC: EMC:EC = 1: 1: 1 v/v) that containing 1.5 wt.% of PVDF as electrolytes and Li-foil was used as anodes. The electrolytes were restricted to 4 ml/g of cathodes in each cell. The commercial celgard 2500 were used as a control separator. The ionic conductivities of the separators were performed on liquid electrolyte-infiltrated separators sandwiched between two stainless steel plates using an electrochemical workstation (Chenhua, CHI 660D, Shanghai) with frequency range between 0.1 Hz and 1 M Hz. The Li∥Li symmetric cells, Li∥Cu asymmetric cells and NCA/Li cells were tested using a battery test system (CT2001A, LAND, China).

Calculations of porosity, electrolyte uptake and ionic conductivity of the ceramic NFs.

The porosity of the membranes was calculated by using equation (1), where M_1 and M_2 are the weight of the separator before and after impregnation in n-butanol, respectively; D_B is the density of n-butanol; V represents the volume of the separators.

$$P = \frac{(M_2 - M_1)}{D_B \times V} \times 100\% \qquad (1)$$

Liquid electrolyte uptakes were measured by soaking the separators in the liquid electrolyte at room temperature. The electrolyte uptake (ω) was calculated using equation (2), where W_1 and W_2 are the weights of the separators before and after immersion in the electrolyte.

$$\omega = \frac{(W_2 - W_1)}{W_1} \times 100\% \qquad (2)$$

The ionic conductivity of separators was measured by electrochemical impedance spectroscopy (EIS). The impedance measurements were performed on liquid electrolyte-soaked separators sandwiched between two stainless steel plates in the frequency range of 10 mHz to 100 kHz. The ionic conductivity σ was calculated using equation (3), where d is the separator thickness, S is the cross-sectional area, and R_b is the bulk resistance obtained from the Nyquist plots.

$$\sigma = \frac{d}{R_b \times S} \qquad (3)$$